Available online at www.sciencedirect.com

jmr&t Journal of Materials Research and Technology

journal homepage: www.elsevier.com/locate/jmrt

Original Article

Multiscale modification of aluminum alloys with deep cryogenic treatment for advanced properties

Matic Jovičević-Klug [a,**], *Levi Tegg* [b,c], *Patricia Jovičević-Klug* [a,d,*], *Goran Dražić* [e], *László Almásy* [f], *Bryan Lim* [b,c], *Julie M. Cairney* [b,c], *Bojan Podgornik* [d]

[a] *Max-Planck Institute for Iron Research, Max-Planck-Str. 1, 40237 Düsseldorf, Germany*
[b] *School of Aerospace, Mechanical and Mechatronic Engineering, The University of Sydney, Camperdown, NSW 2006, Australia*
[c] *Australian Centre for Microscopy and Microanalysis, The University of Sydney, Camperdown, NSW 2006, Australia*
[d] *Institute of Metals and Technology, Lepi Pot 11, 1000 Ljubljana, Slovenia*
[e] *National Institute of Chemistry, Hajdrihova Ulica 19, 1000 Ljubljana, Slovenia*
[f] *Institute for Energy Security and Environmental Safety, Centre for Energy Research, Konkoly Thege Miklos út 29-33, Budapest 1121, Hungary*

ARTICLE INFO

Article history:
Received 3 September 2022
Accepted 19 October 2022
Available online 29 October 2022

Keywords:
Aluminum alloys
Precipitation
Deep cryogenic treatment
Microstructure
Atom probe tomography
Small-angle neutron scattering

ABSTRACT

Deep cryogenic treatment (DCT) has arisen as a promising green technology to modify the properties of metallic materials. Here we present a substantial (55%) improvement to the wear resistance of an Al-Mg-Si alloy using DCT without any deterioration of other mechanical properties. This improvement is attributed to a slight hardness increase resulting from multiscale microstructural modifications. DCT modifies the morphology of dispersoids as well as the organization and morphology of β'' precipitates that increase their fraction (25%) at the expense of β' precipitates. These effects are related to the greater nanoscale mobility and segregation of the alloying elements (Mg, Si) following DCT, resulting from lattice defect recombination. This research provides a fundamental breakthrough in understanding the DCT effect on aluminum alloys, confirming DCT as a feasible CO_2-free treatment step towards improvement of aluminum alloys.

1. Introduction

Al-Mg-Si aluminum alloys, also known as the 6xxx aluminum series, are among the most widely used aluminum alloy series. These alloys exhibit a high resistance to stress and corrosion, good mechanical properties, are straightforward to anodize, and have good formability and weldability. This makes them an excellent choice for applications in the electrical,

* Corresponding author.
** Corresponding author.
E-mail addresses: m.jovicevic-klug@mpie.de (M. Jovičević-Klug), patricia.jovicevicklug@imt.si (P. Jovičević-Klug).
https://doi.org/10.1016/j.jmrt.2022.10.089

aerospace, shipbuilding, and automotive industries (Fig. 1a) [1–3]. These alloys are also highly recyclable and are easily used for the development of crossover aluminum alloys due to their low alloying content and acceptance of minor amounts of uncommon alloying elements [4]. In this respect their mechanical properties can be highly tailored by their chemical composition and heat treatment (i.e age hardening), allowing strengths comparable to the high-strength 7xxx alloys [5–9]. Despite their high mechanical properties, the 6xxx alloys have significantly lower wear resistance as a result of their low hardness (with age hardening peak hardness up to 120 HB) [10]. Anodizing or other coatings can be used to overcome this [11,12]. However, these protective layers can be damaged over time, making the alloys susceptible to long-term wear effects or increased service costs [11]. Bespoke alloy design or treatment processes can be used, but these are energy-intensive [7], and come at the expense of other properties [13]. These issues drive the search for simple and sustainable treatment methods and technologies to improve aluminum alloys throughout their volume, while still maintaining both desirable mechanical properties and good formability.

In regards to tailoring microstructure with heat treatment, a new approach, deep cryogenic treatment (DCT), has been on the rise, which modifies microstructure by exposure to cryogenic temperatures, which consequentially influences the development of final properties of ferrous and non-ferrous alloys [14]. The application and effect of DCT on Al-alloys has been mainly recorded on 5xxx and 7xxx Al-alloys series [15,16], which proves the lack of research of DCT effect on 6xxx series. The authors, which researched Al-alloy in combination to DCT, have reported the decrease in residual stresses [16], increased sub-microscopic precipitation near and at the grain boundaries [16], generation of small and widely dispersed GP-zones [3] and as showed by our previous study Jovicevic-Klug et al., 2022 [17]. DCT induces denser formation of dispersoids and β'' precipitates and growth of β' precipitates. The process of DCT is simple yet effective: aluminum alloys are immersed in liquid nitrogen following homogenization, but before artificial aging. Due to its simplicity, the process can be powered with CO_2-free renewable energy and can be applied to semi-finished or finished products of any shape and form, making this process universal and easily incorporated into industrial processes with minimal environmental impact [14,18].

Based on the literature overview and our previous study, it can be concluded that there is a lack of the understanding and research of DCT effect on 6xxx Al-alloys. As such, EN AW 6026, was selected to be a representative of 6xxx series, due to its chemical composition and application in various industries. With this research we address these demanding conditions with deep cryogenic treatment (DCT), which allows for modification of the aging behavior that leads to a modified microstructure at multiple length scales Furthermore, with this research we also provide an in-depth understanding of how DCT affects Al-Mg-Si aluminum alloys down to the nanoscale, a domain which up until now has remained barely explored in relation to DCT and its possible enhancement with such process. As a result, the findings of this paper provide evidence and understanding of using DCT as a novel tool to substantially improve properties, such as wear resistance, of aluminum alloys without inducing negative consequences to other individual mechanical properties.

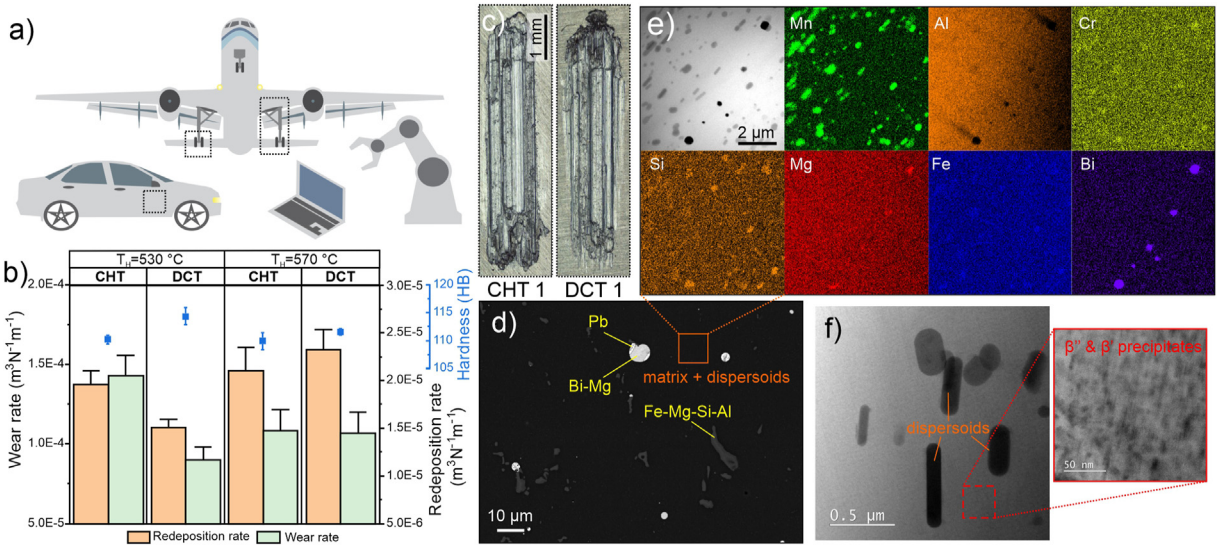

Fig. 1 – (a) Example illustrated applications of Al-Mg-Si alloys in various industries. The dashed squares represent the individual locations of components made of Al-Mg-Si alloys. (b) Wear rate, redeposition rate and hardness results of the aged aluminum alloys with and without deep cryogenic treatment after two different homogenization temperatures T_H. (c) Optical microscopy images showing exemplar wear scars of the conventionally (CHT) and deep cryogenically (DCT) treated aluminum alloy. (d–f) Exemplar (scanning (d) and transmission (e–f)) electron micrographs of the multiphase microstructure displaying a multiscale phase formation that includes: (d) micrometer-scaled intermetallic phases and inclusions, (d) sub-micrometer sized dispersoids enriched with Mn, Si and Fe, and (f) nanometer-sized β'' and β′ precipitates.

2. Methods

2.1. Material, and heat treatment

The commercially available EN AW 6026 alloy, provided by Impol, Slovenia, was used for this research. The chemical composition (in wt.%) of the samples, measured with inductively coupled plasma-optical emission spectrometry using Agilent 720 (Agilent, Santa Clara, CA, USA), is 96.361 Al, 0.7 Mg, 0.68 Si, 0.66 Bi, 0.59 Mn, 0.34 Pb, 0.3 Cu, 0.27 Fe, 0.045 Cr, 0.029 Ti and 0.025 Zn. The treatment procedures and their parameters were selected based on previous experiments presented in our prior publication [17]. Samples of 10 × 10 × 100 mm^3 were machined from the material and homogenized at 570 °C for 1 h in a muffle furnace. Afterwards the samples were extracted from the furnace and quenched in water at 22 °C. The samples were then dried and separated into two groups. The first group, marked as deep cryogenic heat-treated (DCT), was firstly gradually immersed in liquid nitrogen LN_2 (−196 °C) for 24 h. Afterwards the samples were removed from the LN_2 and warmed to room temperature. The corresponding average cooling/warming rate was 10 °C/s, which was determined with temperature measurement of a dummy sample with a K-type thermocouple. Once the samples were warmed, the samples were artificially aged at 190 °C for 8 h using a convection furnace. The other group of samples, marked as conventionally heat treated (CHT), was directly artificially aged under the same conditions as the DCT group.

2.2. Testing of mechanical and wear properties

The hardness was tested according to the Brinell method (SIST EN ISO 6506−1:2014 standard; HBW 2.5/62.5), on the samples using an Innovatest Nexus 7500 device (Innovatest, Selfkant-Heilder, Germany). At least three measurements were made on each sample. Before the measurements, the samples were properly prepared by grinding and polishing. All samples were artificially aged, the hardness was measured after the complete heat treatment.

The testing of wear resistance and coefficient of friction was conducted under reciprocating dry sliding conditions using ball-on-flat contact configuration with a stroke length of 4 mm at home assembled machine. The testing counter body was AISI 52100, Ø32 mm (100Cr6; ~700 HV) favoring predominant abrasive wear. One loading condition was applied, with load 20 N (initial contact pressure of about 400 MPa) and sliding speed 0.01 m/s and frequency of 1 Hz that results to a total sliding distance of 10 m. The measurements were performed 6x for each sample group. The wear volume of the samples was measured using 3D confocal focus variation microscope (Alicona InfiniteFocus, Raaba/Graz, Austria) and the specific wear rate was calculated afterwards based on $k = \frac{W}{F_n \times S}$, where W is wear volume in mm^3, *FN* is normal load in N, and S is sliding distance in m.

2.3. Microscopy

After heat treatment, the samples were metallographically prepared for investigation with scanning electron microscopy. The samples were cut along the middle, polished and their surface finished with colloidal silica (25–40 nm particle size, 15 N load, 3 min polishing time [19]. The microstructural observations were carried out with scanning electron microscopy ZEISS Crossbeam 550 (Zeiss, Oberkochen, Germany) immediately after metallographic preparation. The scanning electron microscopy was conducted with acceleration voltage of 15 kV and working distance of 10 mm. Chemical composition was analyzed by energy-dispersive X-ray spectroscopy (Oxford EDS INCA Energy 450, detector type INCA X-SIGHT LN_2). For transmission electron microscopy (TEM), samples were prepared from 3 mm wide, 1 mm high and 1 mm thick thin foil, prepared from the original samples after treatment. The lamellas were firstly thinned by grinding and polishing using SiC papers to around 100–150 μm thickness. Afterwards, the lamellas were ion-milled using JEOL EM-09100IS Ion Slicer (JEOL, Tokyo, Japan) to electron transparency. For high-resolution atomic investigation, probe Cs corrected Scanning Transmission Electron Microscope (STEM), JEOL ARM 200 CF (JEOL, Tokyo), Japan, equipped with a high-brightness Cold Field Emission Gun (CFEG) operating at 200 kV was used. Qualitative and quantitative elemental chemical analyses were performed with Energy Dispersive X-ray spectroscopy using Jeol Centurio wide-area Silicon Drift Detector (SDD) system.

2.4. Small angle neutron scattering (SANS)

Representatives of both CHT and DCT samples were measured using small-angle neutron scattering (SANS) for evaluation of the precipitation and the size distribution of precipitates. SANS experiments were carried out using the Yellow Submarine diffractometer operating at the Budapest Neutron Center [20]. Samples were attached to a sample changer by adhesive tape and were measured at room temperature. The range of scattering vectors Q was set to 0.016-0.31 $Å^{-1}$, where $Q = 4\ \pi\lambda\ sin\theta$ and 2θ is the scattering angle. In order to access a broad range of Q, we used two different configurations with sample-detector distances 1.15 and 5.125 m. The incident neutron wavelength was set to $\lambda = 4.24$ Å. The raw data have been corrected for sample transmission and room background. Correction to the detector efficiency and conversion of the measured scattering to absolute scale was performed by normalizing the spectra to the scattering from a light water sample.

2.5. Atom probe tomography (APT)

Samples were prepared for atom probe tomography (APT) by sectioning the material into rods of dimensions ≈ 0.5 mm × 0.5 mm × 40 mm. The rods were electropolished to fine tips in two stages: first with 25% perchloric acid in glacial acetic acid, then with 2% perchloric acid in 2-butoxyethanol [21]. Atom probe microscopy was performed using an Imago LEAP 3000X Si, operated in voltage-pulsed mode at 50 K, with a 90 mm path length, 20% pulse fraction, and a 200 kHz pulse rate. The target detection rate varied between 0.5 and 2.0%. Reconstruction was performed using the IVAS module within AP Suite 6.1. The image compression factor (ICF, ξ) was determined by comparing the actual and expected angles between the poles identified on the detector 2D histogram. The field factor (k_f) was determined by comparing the

measured d-spacing along these poles to that predicted from the crystal structure of the Al matrix [21,22]. Isoconcentration surfaces (isosurfaces) were used to calculate proximity histograms (proxigrams) of important solute species [23]. Clustering of solutes was characterized using the DBSCAN algorithm [24–26], as implemented in the IVAS module of AP Suite 6.1. More details of the cluster analysis procedure are included in supplementary information.

3. Results and discussion

With the representative Al-Mg-Si alloy EN AW 6026 we provide clear evidence of substantially greater wear resistance with DCT in contrast to the conventionally heat treated (CHT) counterpart. We found a 55% lower wear rate (Fig. 1b) and shallower wear scars (Fig. 1c) following DCT, when low homogenization temperature is applied (heat treatment 1). This improvement surpasses the wear capabilities of the same alloy when higher homogenization temperatures are used to intentionally promote Si particle formation [17] which improves the wear capabilities of 6xxx alloys [27–29]. Surprisingly, the wear mechanisms remain the same, which display predominant ploughing, plastic adhesion and delamination, regardless of the heat treatment parameters and application of DCT. The effect of DCT on the wear properties with lower homogenization temperature is related to microstructure modifications that lead to a slight improvement in hardness (Fig. 1b), whereas the other mechanical properties are relatively unchanged, as reported in our previous study [17]. The differences originate from the modified reformation of the dispersoids as well as the preferential and denser precipitation of β-type precipitates with the additional cryogenic treatment, while the larger intermetallic phases and inclusions remain unaltered (Fig. 1d). The dispersoids develop a more elongated morphology with DCT (see Fig. 1e and f) compared to those formed with CHT (see Supplementary Fig. 1) with their elongations following the energetically-preferential growth along the <100> direction of the aluminum matrix, as shown previously [17]. Additionally, the chemistry of dispersoids, that is initially set and conserved with CHT as $Al_{15}(Fe,Mn,Cr)_3Si_2$, is also modified with DCT through increasing the Mn content [17]. This change in both the morphology and chemistry of the dispersoids also has a direct impact on the matrix alloying [17] and with it on the precipitation sequence, as confirmed also by Kenyon et al. [30]. The reason for the morphological and chemical changes to the dispersoids with DCT is the reduction of the nucleation barrier due to dislocation motion and recombination resulting from shrinkage pressure during cooling. The dislocations preferentially agglomerate at the interface boundaries of the dispersoids, which lowers the energy barrier for alloying element migration governed by the increased local Peierls stress [31]. Additionally, the gliding dislocations can capture and move lighter alloying elements (such as Si and Mg) through dislocation pipe diffusion [32,33] leaving behind increased concentration of the heavier alloying elements of the partially-dissolved dispersoids that form after homogenization [17]. As a result of both effects, the precipitation behavior of needle-like β-type precipitates is also modified, as discussed below. From this it is clear that microscopic and nanoscopic effects related to the microstructure play an essential role in the wear properties modification with heat treatment and DCT. As such the subtle changes in mechanical properties (i.e. hardness) cannot explain the dramatic improvement of wear resistance changes, suggesting a far deeper relation to the microstructure and nanoscopic changes in the precipitation phenomena of the investigated aluminum alloy.

The transmission electron microscopy (TEM) images presented in Fig. 2 indicate a substantial increase in β'' precipitation with DCT (compare Fig. 2a–e). These are generally aligned along <100> directions, as anticipated from literature and theory [36,37], and exhibit a smaller average diameter (3.9 nm ± 0.8 nm for CHT and 3.5 nm ± 0.85 nm for DCT) and longer lengths (60 nm ± 14.4 nm for CHT and 88 nm ± 20.0 nm for DCT). Furthermore, after DCT the β'' precipitates display a more ordered organization in a 3D perpendicular network compared to the CHT precipitates. This is further supported by the fast Fourier transformation (FFT) pattern, extracted from the DCT TEM micrographs, which indicates a more well-defined and shaper perpendicular (star-like) pattern compared to the CHT variant. The formed precipitates for both samples display generally a semi-coherent state, indicated by the change in the lattice organization with the Al-matrix in Fig. 2c and g (see also inserts), which further support the predominant presence of β'' precipitates for both samples. The strong modification of the precipitation organization is further evidenced through selected area electron diffraction (SAED) of both samples. The CHT sample shows individual small diffraction spots, resulting from the precipitates, that are sporadically formed around the main matrix diffraction spots (Fig. 2d). On the other hand, DCT sample displays a larger number of sporadically positioned smaller diffraction spots as well as an ensemble of diffraction streaks that form a regular rhombic pattern (see Fig. 2h). This pattern overlaps with the main Al diffraction spots, indicating a correlative orientation with the Al-matrix. From the diffraction data it is assumed that the regular positioning of the β'' precipitates lead to the diffraction streaks, whereas the sporadic diffraction spots are mainly formed by the larger β' particles that misorient from the Al-matrix orientation.

The increased precipitation and higher ordering of the precipitates is supported with small-angle neutron scattering (SANS). In comparison to a reference sample without artificial aging, the CHT and DCT samples display an increased presence of particles in the size range of 2–50 nm (Fig. 3), corresponding well to the size of β-type precipitates. The scattering data shows there is~25% increased precipitation with DCT of particles with diameter in the range of 2–10 nm. The 2-D SANS scattering patterns also confirm the anisotropic distribution of the precipitates for both CHT and DCT samples compared to the reference sample. Complementary to the TEM results, the anisotropy is more well defined along 3 perpendicular axes for DCT compared to the CHT alloy. The 3-axial determined anisotropy follows well the theoretical expectation of the precipitate growth and their crystal orientation with the <100> directions of the aluminum matrix [36,37].

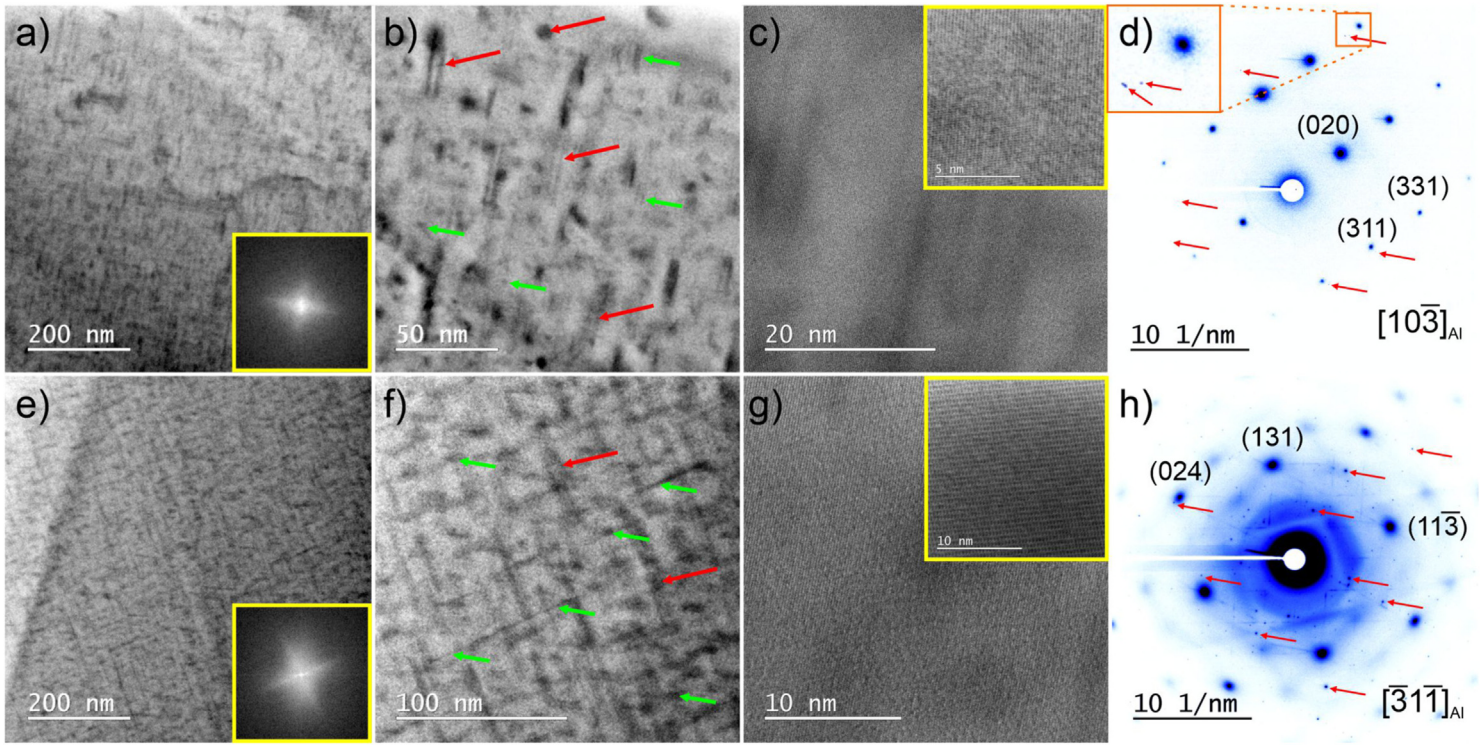

Fig. 2 – Transmission electron images (TEM) of (a–c) CHT and (e–g) DCT samples. In (a) and (e) the inserts display the fast Fourier transformation (FFT) of the presented TEM image, providing textural information about the precipitated particles. The green and red arrows in (b) and (f) indicate the β′ and β'' precipitates, respectively, that are determined based on their structure and dimensions [34,35]. The (d) and (h) display the diffraction pattern of the Al matrix and precipitates. The individual diffraction peaks of precipitates are marked by red arrows.

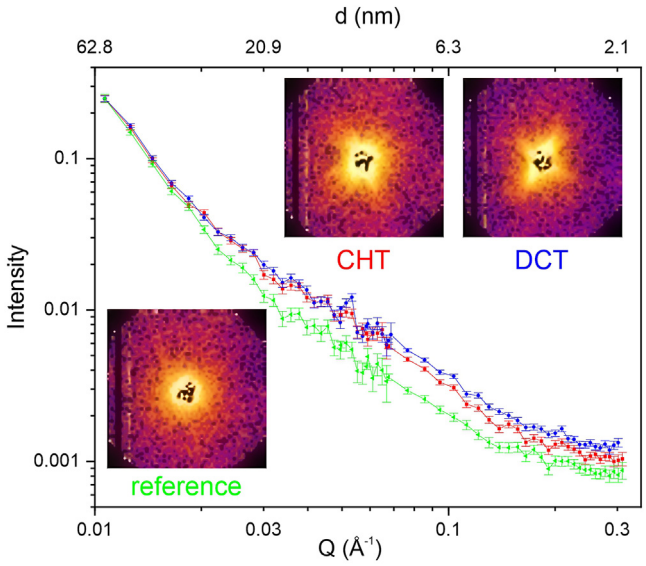

Fig. 3 – Small-angle neutron scattering (SANS) data depicting the intensity in function of the scattering factor Q for the differently treated samples. The Q-derived distance $d = 2\pi/Q$ Mis given in the upper abscissa. The reference sample represents the state of the material before the treatment. The additional 2-D scattering patterns provide evidence in the different anisotropy present for conventionally (CHT) and deep cryogenically (DCT) heat-treated sample compared to the reference sample.

The atom probe tomography (APT) data in Fig. 4 provides a 3D understanding of the distribution of the precipitate elements after CHT and DCT. Fig. 4a and c shows reconstructed atom positions for Al, Si, Mg and Cu, and Fig. 4b and d illustrate the precipitates by using an iso-concentration surface (isosurface) of (Mg,Si) at 5 at.%. For both samples, the precipitates are enriched with Mg and Si as anticipated for the β-type precipitates [35,36,38,39]. However, the precipitates also display a significant enrichment with Cu. Proximity histograms (proxigrams) measure chemical gradients across isosurfaces, and are shown in Fig. 4e–i. The precipitates have a relatively diffuse boundary which extends up to 1 nm into the precipitates, though this may be a result of trajectory aberrations [21]. The composition is similar between the two sample types. Beyond this depth, the DCT precipitates display 50–100% more Mg, 25% more Si, and 100% more Cu alloying than the CHT precipitates (Fig. 4e–g). As a result, the DCT precipitates display on average a cumulative alloying with Mg, Si and Cu of around 75%, whereas the DCT precipitates have only around 50%. The DCT precipitates have a composition suggesting they are of $Al_4Mg_5Si_4$ type, whereas the precipitates in the CHT sample do not follow any known stoichiometry, though this has been observed in previous atom probe studies of Al-Mg-Si alloys [40]. However, comparing just the Mg and Si content and disregarding of the Al values, the precipitates of both samples follow the general composition of β'' precipitates [34,41] with the Mg:Si ratio equal to 1:1 and 1.3:1 for CHT and DCT sample, respectively. With the additional consideration of Cu, the precipitates have a composition of $Mg_4Si_{3.4}Cu_{0.6}$ and $Mg_4Si_{3.2}Cu_{0.8}$ for CHT and DCT sample, respectively, which can be conjointly described by the Cu-rich β'' precipitate variant (named also C precipitate) with chemical composition of Mg_4AlSi_{3+x} Cu_{1-x} [34,42].

The chemical composition in the matrix around the larger precipitates differs between the CHT and DCT samples. Fig. 5 shows the concentration ratio $C_{CHT}/(C_{CHT} + C_{DCT})$ for the proxigram of the solute elements shown in Fig. 4g–i. Values > 0.5 indicate the element is more enriched in the CHT sample at a given position, and <0.5 indicating it is more enriched in the DCT sample at a given position. In the CHT sample, the Mg is enriched in the matrix around the precipitates, whereas for DCT the Mg diffusion has progressed further and the precipitates themselves are Mg-enriched. This suggests that Mg is the main element that influences the precipitation behavior through DCT activated preferential diffusion of Mg from the matrix to the precipitates. Deeper in the matrix, the Mg content is similar for both CHT and DCT samples. In contrast, Si and Cu show enrichment in the matrix and in the precipitates of DCT sample compared to CHT. Si and Cu are of approximately equal concentration at the matrix-precipitate interface. The general enrichment of the DCT sample with Si and Cu (see Supplementary Table 1) is postulated to originate from the DCT induced changes of the dispersoids. It should be noted that the surrounding matrix of the precipitates displays their local surrounding and enrichment caused by the growth of the precipitates and can be understood as a halo effect of the diffusion of alloying elements towards the precipitates. This is clear by comparing the values of the surrounding matrix with the values of the analyzed bulk matrix, presented in the Supplementary Table 1. The increased enrichment effect of precipitates with DCT is also further proven with background-corrected composition of the precipitates, presented in Supplementary Table 1, extracted via cluster analysis.

Although the analysis volume of atom probe is small, it suggests that the CHT sample contained a greater number of very large (>1000 ions) precipitates compared to the DCT sample (see Supplementary Fig. 2) and that the DCT sample has a larger number of precipitates, which is consistent with TEM and SANS results.

Cluster analysis on the atom probe data, performed using the DBSCAN algorithm [26], was used to study the morphology of the precipitates (Fig. 6a and b, Supplementary Information Figs. 2–4). It was found that precipitates in the DCT sample have cross-sectional aspect ratio (i.e., y/z) of around 1.5, whereas those in the CHT sample range between 1 and 3, indicating a more oval structure compared to the rounder DCT precipitates. There was no relationship between the aspect ratio and the size of the cluster, but there seems to be a weak link between aspect ratio, Cu content and treatment type, where low-Cu precipitates in the CHT sample were generally more ribbon-like, whereas for DCT sample the precipitates are closer to spherical, irrespective of the different Cu content. Consistent with the proxigrams in Fig. 3e–i, there is clear alloying of the precipitates with Si and Mg in the DCT sample (Fig. 6d–f). Furthermore, Si and Mg enrichment tend to occur together, having a linear relationship, particularly for larger clusters that have a Mg:Si ratio above 1. The Cu content of the DCT precipitates display a broader distribution compared to a fairly tight distribution in the CHT sample, where Cu content is around 0.5% (Fig. 6g–i).

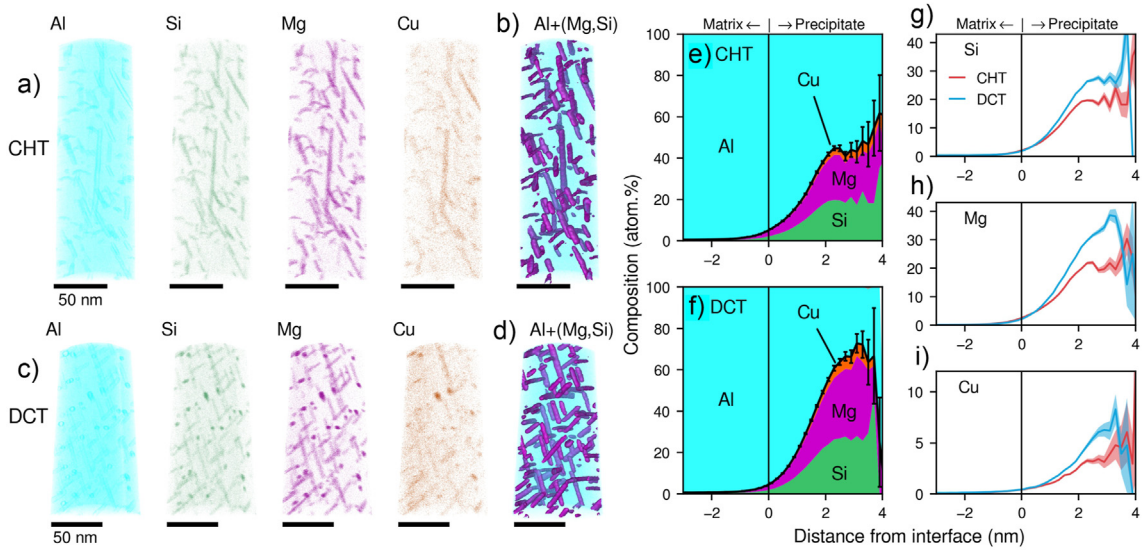

Fig. 4 – Atom probe tomography (APT) reconstruction and analysis, based on the reconstructed Al, Si, Mg and Cu positions for the (a) CHT and (c) DCT dataset. Isoconcentration surfaces (isosurfaces) of (Mg,Si) at 5 at.% (purple rods) are shown against Al positions (blue dots) in (b,d). Proximity histograms (proxigrams) over the entire isosurfaces in (b) and (d) are shown for (e) the CHT sample and (f) the DCT sample as stack plots, with the sum of the solute elements (Si, Mg and Cu) shown as a thick black line with the error bars calculated from the sum of the uncertainties of the solute elements profiles. Positive distances move into the precipitate, and negative distances into the matrix. (g–i) show Individual profiles for solute elements, comparing the CHT and DCT samples, with shaded regions indicating uncertainties.

By comparing the volumes of the clusters and the remaining matrix, the precipitate volume fractions can be estimated as 37.1% and 35.6% for the CHT and DCT samples, respectively. The APT data suggests that the volume fraction off the precipitates does not significantly change with DCT, only the number density of the precipitates. This is consistent with the theoretical expectation of the precipitation volume yield being set by the ageing temperature and time [37,43,44], whereas the precipitation density and morphological reformation can be assigned to the implementation of DCT.

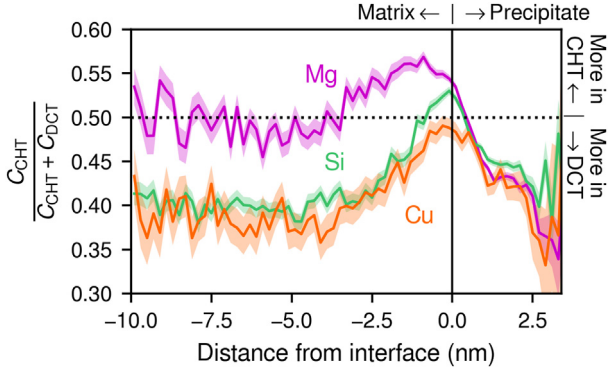

Fig. 5 – Proxigrams showing the ratio $A_{CHT}/(A_{CHT}+A_{DCT})$ of solute species, allowing comparison between CHT and DCT results. Ratio values > 0.5 indicate that species is more enriched in that location in the CHT sample; <0.5 in the DCT sample. Positive distances indicate the precipitate, negative distances the matrix.

3.1. *DCT mechanism - influence on precipitation*

This microstructural and chemical investigation shows a significant difference in the morphology and distribution of the precipitates after DCT, and this can explain the improved wear resistance of DCT samples. On this matter, it should be clear that reinforcement of the material can yield proportionally lower effect on the macro hardness than on the wear properties. This means that the Archard law [45] (the scaling of wear resistance with higher hardness) on a macroscopic level is not applicable. The improved regularity and the increased density of precipitates creates a dense precipitate network. Due to their regular distribution and size, it is postulated that the precipitates function as a composite filler in a matrix structure. As a result of the rounded morphology and coherency with the matrix, the precipitates lead to a homogeneous stress field without imposing any stress concentrations, leading to improved strength and hardness without detrimental effects to the elasticity and fracturing of the alloy [17]. As a result, the cohesion of the material and stress state regularity within the material will play a dominant role on the wear resistance of the material, since soft metals such as aluminum are prone to tearing and delamination wear behavior due to the high plastic behavior of such materials [46]. Furthermore, the precipitation changes result in higher integrity and cohesion of the matrix, leading to the substantially improved resistance to tearing during wear, thus significantly improving the wear resistance. This effect can be correlated with the slight increase in hardness that is generally a result of the matrix reinforcement that modifies the matrix strength and consequentially the resistance to tearing

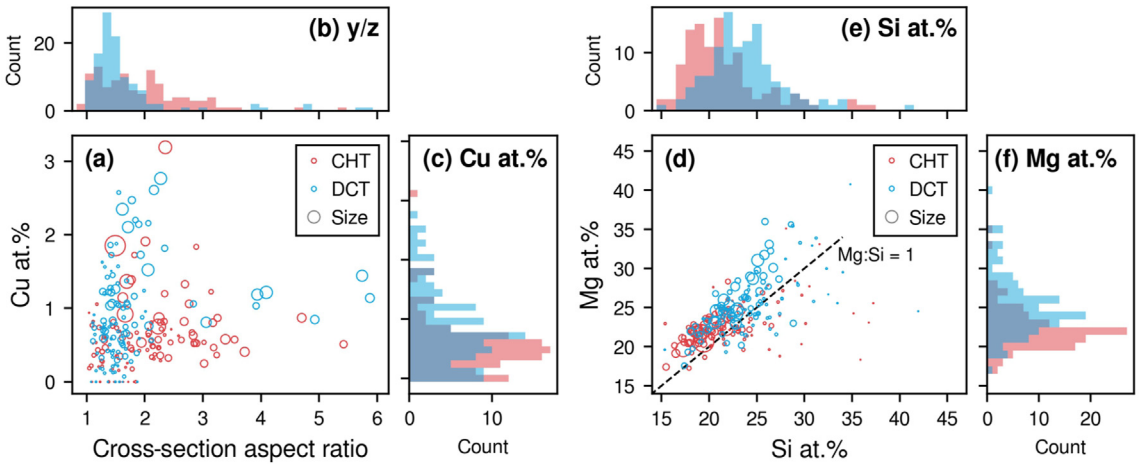

Fig. 6 – 1D and 2D histograms of some morphological and chemical descriptors of (Mg,Si) clusters found using APT. (a) Scatter plot of the cross-sectional aspect ratio (i.e., y/z) against the Cu at.% content of each cluster, with (b) and (c) showing histograms of these quantities respectively. (d) Scatter plot of the Si at.% and Mg at.% content of each cluster, with (b) and (c) showing histograms of these quantities respectively. The dark dashed line represents the 1:1 ratio guideline of the Mg:Si ratio. In (a) and (d), the area of the dots is proportional to the number of ranged ions in the cluster.

and fracturing [17]. With such features, the aluminum alloy displays increased resistivity to wear through direct matrix reinforcement with precipitates, which effectively counter-attacks also higher values of imposed stress and material tearing, leading to shallower wear scars as well as material redeposition as observed from the wear tests provided in Fig. 1b and c.

To explain the modification to the precipitates following DCT, we propose a two-part mechanism: the first is related to an increase in dislocation density with DCT, and the second to the potential energy difference caused by compressive stress build-up in the matrix material with DCT. The first part, sketched in Fig. 7a, assumes that the dislocation density of the aluminum alloy increases with the exposure of the material to cryogenic temperatures. This assumption stems from the imposed shrinkage pressures generated with the cooling of the material, which in turn activates non-diffusional dislocation generation and recombination. It should be noted that for aluminum alloys displaying natural aging direct measurement of dislocation density using TEM cannot be performed, as natural aging commences immediately after samples are raised from cryogenic temperatures. Nevertheless, the increased dislocation density after DCT has been confirmed for several metallic materials, including other aluminum alloys [47–50]. With the movement and recombination of dislocations, we propose that the lighter alloying elements are dragged by dislocations and agglomerated on them through pipe diffusion [32,33]. As a result, the dislocations act as sinks for the solute atoms (Mg and Si) that are extracted from positions of dispersoids and other intermetallic regions that have larger concentrations of solute atoms. Of course, the dislocation agglomeration of alloying elements can only explain the irregular formation of the precipitates that cannot be formed in a regular pattern through dislocations. Instead, this mechanism only explains the denser presence of slightly misaligned precipitates that show diverted orientations from the main crystallographic directions of the aluminum matrix (see diffraction pattern in Fig. 2h). The improved regularity and increased density of the precipitation results from the cryogenically-activated shrinkage pressure. This shrinkage pressure also causes build-up of compressive stresses in the matrix that results in lattice contraction and vacancy redistribution, as sketched in Fig. 7b. The resulting lattice displacement leads to a shorter nearest neighbor distance, resulting in a decreased Peierls potential [31]. This lowers the energy barrier for solute atoms to move from site to site and increases their likelihood of agglomerating into clusters around vacancies, which act as embryo nucleation precursors [51]. The clusters can thus form more homogeneously and evolve into the β'' precipitates more quickly (see Fig. 7c). This leads to solute depletion in the local matrix as well as more defined alloying of the precipitates with aging time compared to the CHT samples. Furthermore, as the nucleation and growth energies are similar for mostly all precipitates, their evolution is more uniform and monotonic compared to the CHT variant, resulting in a larger regularity of the precipitates from both morphological as well as distributional perspective. In contrast, the CHT sample will develop the precipitates in an irregular fashion due to the variable scaling of the local energy potentials caused by local stress variations, solute atoms random agglomeration, and vacancy distribution formed during the quenching procedure. It should be noted that the dislocation-based nucleation is present for both samples as dislocations have a high affinity towards solute atom agglomeration and display a low potential energy for precipitate nucleation [51,52]. As a result, the slight modification of the orientation of the precipitates occurs for both samples. The discrepancy from the orthogonal positioning from the principal <100> directions of the matrix is supported by the TEM SAED that display individual precipitate diffraction spots not superimposed with the main diffraction spots of the matrix (Fig. 2h). However, due to the

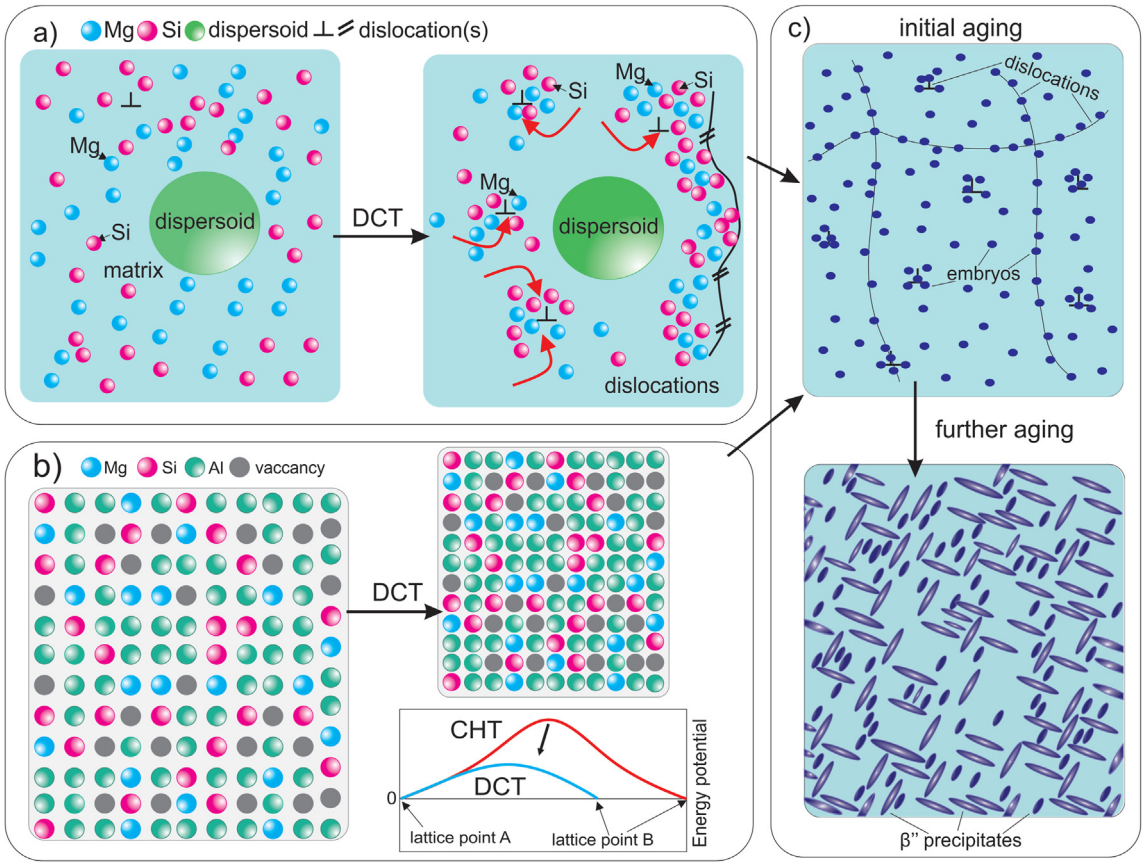

Fig. 7 – (a) schematic representation of solute atom agglomeration around dislocations with deep cryogenic treatment (DCT) induced by the gliding dislocation motion and pipe diffusion [32,33] (b) Schematic representation of the lattice shrinkage with DCT that induces changes in the energy potential between neighboring lattice points, indicated by the simplified energy diagram below. (c) Schematic representation of the resulting formation of embryos forming based on the conjoined effect of both mechanisms presented in (a) and (b) in the initial part of the artificial aging process. The lower image presents the final microstructure with β'' precipitates after artificial aging that obscures the prior preferential formation of embryos.

increased density of the precipitates with DCT, the ordering and even distribution of precipitates is overall more regular, which directly improve the matrix reinforcement effect of the precipitates, resulting in the substantial improvement in the materials wear resistance.

With the new understanding of DCT on the precipitation behavior, it is possible to utilize this approach to engineer the multiscale modification of aluminum alloys in order to tailor mechanical properties. It is proposed that DCT inhibits premature precipitate growth from the local inhomogeneities of the system, and instead shifts the precipitation energetics to produce more homogeneous precipitation. In a comparative sense, DCT similarly impairs the negative effect of natural aging on the precipitation evolution and loss of maximum hardness with sequential artificial aging [37,51,53] as achieved with pre-heating [37], up-quenching [54] and lean alloy design [35]. However, unlike most previous processes, DCT does not require input of thermal energy, thus making it industrially more clean with no CO_2 emission as the production of liquid nitrogen is achievable through long-lasting and sustainable green energy refrigeration technology with no waste production [55]. This is supported by the increased interest in cryogenic storage and utilization of cryogenics as green energy carriers [55] that has resulted in the establishment of multinational projects, such as CryoHub [56]. Furthermore, DCT does not require changes to the alloying design thus making the process applicable to a range of Al-Mg-Si alloys as well as other aluminum alloy series [15,16,57] without sacrificing their properties, functionality and applicability. Additionally, DCT modifies the stress state of the matrix and alters the reformation of the dispersoids during aging, which can further tailor individual properties of aluminum alloys [17,30,57,58].

3.2. *Conclusions*

In this research the impact of DCT on wear properties of Al-Mg-Si aluminum alloy is disclosed and correlated to individual microstructural changes that develop on several length scales. DCT modifies the changes the formation and density of dispersoids as well as precipitates, at which both develop preferential elongation along the <100> directions of the aluminum matrix. We disclose that the resulting changes to the agglomeration tendency of solute atoms after DCT through dislocation and stress state changes, directly

influence the nucleation and growth of β-type precipitates. As a result, the precipitation capabilities of the β'' precipitates improve with DCT, which also results in a higher alloying of them. Additionally, due the improved nucleation capability of precipitates, DCT increases the precipitation density and regularity of the precipitation across the matrix, which further improves the homogeneity of the material. The resulting changes consequentially act on the strengthening of the matrix, which improves from both the overall influence of the precipitates on the matrix through their smaller-size, denser presence, higher regularity and higher alloying content. With the presented results, we envision that the DCT processing of aluminum alloys displays a viable, green and economically interesting sub-process to develop aluminum alloys with advanced properties interesting for a range of industries such automotive, robotic and aeronautic industry.

CRediT authorship contribution statement

M.J.-K., L.T. and P.J-K. designed the experiments and analyzed the results. M.J.-K. performed tribological testing. L.T. and B.L. performed APT experiments under the supervision of J.M.C. P.J.-K. prepared the samples for all analyses. G.D. performed TEM imaging and analysis. L.A. performed SANS analysis. G.D. and L.A. provided description of methodology part for specific measurements. This paper was written by M.J.-K., L.T. and P.J-K. All authors contributed to the general discussions and reviewed the paper. All authors have read and agreed to the published version of the manuscript.

Funding

This work was supported by Slovenian Research Agency (ARRS), Ljubljana, Slovenia [No. P2-0050]. Authors P.J-K., M.J-K. and B.P. would like to acknowledge Budapest Neutron Center, for providing beamtime at its neutrons scattering facilities and for financial support of project BRR¬-639. Authors L.T. and J.M.C. would like to acknowledge the Australian Research Council (ARC) [Future Fellowship FT180100232]. The contributions of author B.L. was sponsored by the Department of Industry, Innovation and Science under the auspices of the AUSMURI program.

Data availability

The raw/processed data required to reproduce these findings cannot be shared at this time as the data also forms part of an ongoing study.

Declaration of Competing Interest

The authors declare that they have no known competing financial interests or personal relationships that could have appeared to influence the work reported in this paper.

Acknowledgement

The authors acknowledge the technical and scientific assistance of Institute of Metals and Technology, Slovenia and Sydney Microscopy & Microanalysis, the University of Sydney node of Microscopy Australia. B.L. acknowledges helpful discussions and supervision by Prof. S.P. Ringer (University of Sydney).

Appendix A. Supplementary data

Supplementary data to this article can be found online at https://doi.org/10.1016/j.jmrt.2022.10.089.

REFERENCES

[1] Park DH, Choi SW, Kim JH, Lee JM. Cryogenic mechanical behavior of 5000- and 6000-series aluminum alloys: issues on application to offshore plants. Cryogenics 2015;68:44–58. https://doi.org/10.1016/j.cryogenics.2015.02.001.

[2] Lech-Grega M, Szymański W, Płonka B, Boczkal S, Gawlik M, Bigaj M, et al. The structure and properties of wrought aluminium alloys series 6xxx with vanadium for automotive industry. In: Light metals 2013. Hoboken, NJ, USA: John Wiley & Sons; 2013. p. 527–32. https://doi.org/10.1002/9781118663189.ch90.

[3] Steier VF, Ashiuchi ES, Reißig L, Araújo JA. Effect of a deep cryogenic treatment on wear and microstructure of a 6101 aluminum alloy. Adv Mater Sci Eng 2016:2016. https://doi.org/10.1155/2016/1582490.

[4] Raabe D, Ponge D, Uggowitzer PJ, Roscher M, Paolantonio M, Liu C, et al. Making sustainable aluminum by recycling scrap: the science of "dirty" alloys. Prog Mater Sci 2022;128:100947. https://doi.org/10.1016/j.pmatsci.2022.100947.

[5] Das SK, Felberbaum M. US20180119261A1 - high strength 6xxx series aluminum alloys and methods of making the same. 2017. https://patents.google.com/patent/US20180119261A1/en. [Accessed 20 May 2022]. accessed.

[6] Steinacher M. Microstructure and properties of a novel Al-Mg-Si alloy AA 6086. Metals 2021;11:368. https://doi.org/10.3390/met11020368.

[7] Hu J, Zhang W, Fu D, Teng J, Zhang H. Improvement of the mechanical properties of Al-Mg-Si alloys with nano-scale precipitates after repetitive continuous extrusion forming and T8 tempering. J Mater Res Technol 2019;8:5950–60. https://doi.org/10.1016/j.jmrt.2019.09.070.

[8] Yu JM, Hashimoto T, Li HT, Wanderka N, Zhang Z, Cai C, et al. Formation of intermetallic phases in unrefined and refined AA6082 Al alloys investigated by using SEM-based ultramicrotomy tomography. J Mater Sci Technol 2022;120:118–28. https://doi.org/10.1016/j.jmst.2022.02.007.

[9] Han Y, Ma K, Li L, Chen W, Nagaumi H. Study on microstructure and mechanical properties of Al-Mg-Si-Cu alloy with high manganese content. Mater Des 2012;39:418–24. https://doi.org/10.1016/j.matdes.2012.01.034.

[10] ASM handbook volume 2: properties and selection: nonferrous alloys and special-purpose materials. ASM International; 1990. https://www.asminternational.org/search/-/journal_content/56/10192/06182G/PUBLICATION. [Accessed 20 May 2022]. accessed.

[11] Udoye NE, Fayomi OSI, Inegbenebor AO. Assessment of wear resistance of aluminium alloy in manufacturing industry-a

review. In: Procedia manuf. Elsevier B.V.; 2019. p. 1383–6. https://doi.org/10.1016/j.promfg.2019.09.007.
[12] Liu W, Luo Y, Sun L, Wu R, Jiang H, Liu Y. Fabrication of the superhydrophobic surface on aluminum alloy by anodizing and polymeric coating. Appl Surf Sci 2013;264:872–8. https://doi.org/10.1016/j.apsusc.2012.10.167.
[13] Jin H, Guan R, Huang X, Fu Y, Zhang J, Chen X, et al. Understanding the precipitation mechanism of copper-bearing phases in Al-Mg-Si system during thermo-mechanical treatment. J Mater Sci Technol 2022;96:226–32. https://doi.org/10.1016/j.jmst.2021.04.026.
[14] Jovičević-Klug P, Podgornik B. Review on the effect of deep cryogenic treatment of metallic materials in automotive applications. Metals 2020;10:434. https://doi.org/10.3390/met10040434.
[15] Gao W, Wang X, Chen J, Ban C, Cui J, Lu Z. Influence of deep cryogenic treatment on microstructure and properties of 7A99 ultra-high strength aluminum alloy. Metals 2019;9:631. https://doi.org/10.3390/met9060631.
[16] Bouzada S, Cabeza M, Merino P, Trillo. Effect of deep cryogenic treatment on the microstructure of an aerospace aluminum alloy. Adv Mater Res 2012;445:965–70. https://doi.org/10.4028/www.scientific.net/AMR.445.965.
[17] Jovičević-Klug M, Rezar R, Jovičević-Klug P, Podgornik B. Influence of deep cryogenic treatment on natural and artificial aging of Al-Mg-Si alloy EN AW 6026. J Alloys Compd 2022;899:163323. https://doi.org/10.1016/j.jallcom.2021.163323.
[18] Cryogenic treatment | increase the lifespan of ALL metal parts | CTP cryogenics, (n.d.). https://ctpcryogenics.com/. [Accessed 5 August 2022]. accessed.
[19] Jovičević-Klug P, Lipovšek N, Jovičević-Klug M, Podgornik B. Optimized preparation of deep cryogenic treated steel and Al-alloy samples for optimal microstructure imaging results. Mater Today Commun 2021;27:102211. https://doi.org/10.1016/J.MTCOMM.2021.102211.
[20] Almásy L. New measurement control software on the Yellow submarine SANS instrument at the budapest neutron centre. Journal of Surface Investigation 2021;15:527–31. https://doi.org/10.1134/S1027451021030046.
[21] Gault B, Moody MP, Cairney JM, Ringer SP. Atom probe microscopy. New York, NY, USA: Springer; 2012. https://doi.org/10.1007/978-1-4614-3436-8.
[22] Gault B, Moody MP, de Geuser F, Tsafnat G, la Fontaine A, Stephenson LT, et al. Advances in the calibration of atom probe tomographic reconstruction. J Appl Phys 2009;105:034913. https://doi.org/10.1063/1.3068197.
[23] Hellman OC, Vandenbroucke JA, Rüsing J, Isheim D, Seidman DN. Analysis of three-dimensional atom-probe data by the proximity histogram. Microsc Microanal 2000;6:437–44. https://doi.org/10.1007/s100050010051.
[24] Marceau RKW, Stephenson LT, Hutchinson CR, Ringer SP. Quantitative atom probe analysis of nanostructure containing clusters and precipitates with multiple length scales. Ultramicroscopy 2011;111:738–42. https://doi.org/10.1016/j.ultramic.2010.12.029.
[25] Larson DJ, Prosa TJ, Ulfig RM, Geiser BP, Kelly TF. Local electrode atom probe tomography. New York: Springer; 2013. https://doi.org/10.1007/978-1-4614-8721-0.
[26] Vaumousse D, Cerezo A, Warren PJ. A procedure for quantification of precipitate microstructures from three-dimensional atom probe data. Ultramicroscopy 2003;95:215–21. https://doi.org/10.1016/S0304-3991(02)00319-4.
[27] Shivaramu HT, Umashankar KS, Prashantha DA. Wear characteristics comparison of cast and powder metallurgy based Al and Al-Si alloy [LM6]. In: Mater today proc. Elsevier; 2018. p. 8138–46. https://doi.org/10.1016/j.matpr.2017.11.501.
[28] Singh M, Prasad BK, Mondal DP, Jha AK. Dry sliding wear behaviour of an aluminium alloy-granite particle composite. Tribol Int 2001;34:557–67. https://doi.org/10.1016/S0301-679X(01)00046-9.
[29] Shabel BS, Granger DA, Truckner WG. Friction and wear of aluminum-silicon alloys. In: ASM handbook: friction, lubrication, and wear technology; 1992. p. 785–94. https://doi.org/10.1361/asmhba0002331.
[30] Kenyon M, Robson J, Fellowes J, Liang Z. Effect of dispersoids on the microstructure evolution in Al – Mg – Si alloys. Adv Eng Mater 2019;21:1800494. https://doi.org/10.1002/adem.201800494.
[31] Lu G. The Peierls—Nabarro model of dislocations: a venerable theory and its current development. In: Handbook of materials modeling. Springer Netherlands; 2005. p. 793–811. https://doi.org/10.1007/978-1-4020-3286-8_41.
[32] Xie R, Lu S, Li W, Tian Y, Vitos L. Dissociated dislocation-mediated carbon transport and diffusion in austenitic iron. Acta Mater 2020;191:43–50. https://doi.org/10.1016/j.actamat.2020.03.042.
[33] Picu RC, Zhang D. Atomistic study of pipe diffusion in Al-Mg alloys. Acta Mater 2004;52:161–71. https://doi.org/10.1016/j.actamat.2003.09.002.
[34] Andersen SJ, Marioara CD, Friis J, Wenner S, Holmestad R. Precipitates in aluminium alloys. Adv Phys X 2018;3:1479984. https://doi.org/10.1080/23746149.2018.1479984.
[35] Lai YX, Jiang BC, Liu CH, Chen ZK, Wu CL, Chen JH. Low-alloy-correlated reversal of the precipitation sequence in Al-Mg-Si alloys. J Alloys Compd 2017;701:94–8. https://doi.org/10.1016/j.jallcom.2017.01.095.
[36] Lai YX, Fan W, Yin MJ, Wu CL, Chen JH. Structures and formation mechanisms of dislocation-induced precipitates in relation to the age-hardening responses of Al-Mg-Si alloys. J Mater Sci Technol 2020;41:127–38. https://doi.org/10.1016/j.jmst.2019.11.001.
[37] Zandbergen MW, Xu Q, Cerezo A, Smith GDW. Study of precipitation in Al-Mg-Si alloys by Atom Probe Tomography I. Microstructural changes as a function of ageing temperature. Acta Mater 2015;101:136–48. https://doi.org/10.1016/j.actamat.2015.08.017.
[38] Vissers R, van Huis MA, Jansen J, Zandbergen HW, Marioara CD, Andersen SJ. The crystal structure of the β′ phase in Al-Mg-Si alloys. Acta Mater 2007;55:3815–23. https://doi.org/10.1016/j.actamat.2007.02.032.
[39] Robson JD, Engler O, Sigli C, Deschamps A, Poole WJ. Advances in microstructural understanding of wrought aluminum alloys. Metall Mater Trans 2020;51(9):4377–89. https://doi.org/10.1007/S11661-020-05908-9. 51 (2020).
[40] Hasting HS, Frøseth AG, Andersen SJ, Vissers R, Walmsley JC, Marioara CD, et al. Composition of B″ precipitates in Al-Mg-Si alloys by atom probe tomography and first principles calculations. J Appl Phys 2009;106:123527. https://doi.org/10.1063/1.3269714.
[41] Saito T, Mørtsell EA, Wenner S, Marioara CD, Andersen SJ, Friis J, et al. Atomic structures of precipitates in Al-Mg-Si alloys with small additions of other elements. Adv Eng Mater 2018;20:1800125. https://doi.org/10.1002/adem.201800125.
[42] Torster M, Ehlers FJH, Marioara CD, Andersen SJ, Holmestad R. Applying precipitate-host lattice coherency for compositional determination of precipitates in Al-Mg-Si-Cu alloys. Phil Mag 2012;92:3833–56. https://doi.org/10.1080/14786435.2012.693214.
[43] Werinos M, Antrekowitsch H, Kozeschnik E, Ebner T, Moszner F, Löffler JF, et al. Ultrafast artificial aging of Al-Mg-Si alloys. Scripta Mater 2016;112:148–51. https://doi.org/10.1016/j.scriptamat.2015.09.037.
[44] Poznak A, Marceau RKW, Sanders PG. Composition dependent thermal stability and evolution of solute clusters in Al-Mg-Si analyzed using atom probe tomography. Mater

Sci Eng 2018;721:47–60. https://doi.org/10.1016/j.msea.2018.02.074.
[45] Archard JF. Contact and rubbing of flat surfaces. J Appl Phys 1953;24:981–8. https://doi.org/10.1063/1.1721448.
[46] Subramanian C. Wear properties of aluminium-based alloys. In: Surface engineering of light alloys: aluminium, magnesium and titanium alloys. Elsevier; 2010. p. 40–57. https://doi.org/10.1533/9781845699451.1.40.
[47] Antony A, Schmerl NM, Sokolova A, Mahjoub R, Fabijanic D, Stanford NE. Quantification of the dislocation density, size, and volume fraction of precipitates in deep cryogenically treated martensitic steels. Metals 2020;10:1561. https://doi.org/10.3390/met10111561.
[48] Dong F, Yi Y, Huang C, Huang S. Influence of cryogenic deformation on second-phase particles, grain structure, and mechanical properties of Al–Cu–Mn alloy. J Alloys Compd 2020;827:154300. https://doi.org/10.1016/j.jallcom.2020.154300.
[49] Jia J, Meng M, Zhang Z, Yang X, Lei G, Zhang H. Effect of deep cryogenic treatment on the microstructure and tensile property of Mg-9Gd-4Y–2Zn-0.5Zr alloy. J Mater Res Technol 2022;16:74–87. https://doi.org/10.1016/j.jmrt.2021.11.137.
[50] Dong Z, Fei X, Gong B, Zhao X, Nie J. Effects of deep cryogenic treatment on the microstructure and properties of rolled Cu foil. Materials 2021;14:5498. https://doi.org/10.3390/ma14195498.
[51] Yang Z, Banhart J. Natural and artificial ageing in aluminium alloys – the role of excess vacancies. Acta Mater 2021;215:117014. https://doi.org/10.1016/j.actamat.2021.117014.
[52] Takeyama T, Koda S. Preferred precipitation on dislocation lines in an aluminium alloy. Nature 1957;179:777–8. https://doi.org/10.1038/179777b0.
[53] Werinos M, Antrekowitsch H, Ebner T, Prillhofer R, Uggowitzer PJ, Pogatscher S. Hardening of Al-Mg-Si alloys: effect of trace elements and prolonged natural aging. Mater Des 2016;107:257–68. https://doi.org/10.1016/j.matdes.2016.06.014.
[54] Schmid F, Dumitraschkewitz P, Kremmer T, Uggowitzer PJ, Tosone R, Pogatscher S. Enhanced aging kinetics in Al-Mg-Si alloys by up-quenching. Communications Materials 2021;2(1):1–12. https://doi.org/10.1038/s43246-021-00164-9. 2 (2021).
[55] Li Y, Chen H, Zhang X, Tan C, Ding Y. Renewable energy carriers: hydrogen or liquid air/nitrogen? Appl Therm Eng 2010;30:1985–90. https://doi.org/10.1016/j.applthermaleng.2010.04.033.
[56] Liquid air could store renewable energy and reduce emissions - IEEE spectrum (n.d.), https://spectrum.ieee.org/liquid-air-could-store-renewable-energy-and-cut-food-industry-emissions. [Accessed 23 June 2022].
[57] Araghchi M, Mansouri H, Vafaei R, Guo Y. A novel cryogenic treatment for reduction of residual stresses in 2024 aluminum alloy. Mater Sci Eng 2017;689:48–52. https://doi.org/10.1016/j.msea.2017.01.095.
[58] Wei L, Wang D, Li H, Xie D, Ye F, Song R, et al. Effects of cryogenic treatment on the microstructure and residual stress of 7075 aluminum alloy. Metals 2018;8:273. https://doi.org/10.3390/MET8040273.